A&A 537, A94 (2012)
DOI: 10.1051/0004-6361/201118097

Astronomy & Astrophysics

The ultracool dwarf DENIS-P J104814.7-395606

Chromospheres and coronae at the low-mass end of the main-sequence

B. Stelzer[1], J. Alcalá[2], K. Biazzo[2], B. Ercolano[3], I. Crespo-Chacón[4], J. López-Santiago[4], R. Martínez-Arnáiz[4], J. H. M. M. Schmitt[5], E. Rigliaco[6], F. Leone[7], and G. Cupani[8]

[1] INAF – Osservatorio Astronomico di Palermo, Piazza del Parlamento 1, 90134 Palermo, Italy
e-mail: stelzer@astropa.inaf.it
[2] INAF - Osservatorio Astronomico Capodimonte, Salita Moiariello 16, 80131 Napoli, Italy
[3] Universitätssternwarte München, Scheinerstrasse 1, 81679 München, Germany
[4] Dpto. de Astrofísica y Ciencias de la Atmósfera, Universidad Complutense de Madrid, 28040 Madrid, Spain
[5] Hamburger Sternwarte, Gojenbergsweg 112, 21029 Hamburg, Germany
[6] Lunar and Planetary Laboratory, University of Arizona, 1629 E. University Blvd, AZ 85721 Tucson, USA
[7] INAF - Osservatorio Astronomico di Catania, via S.Sofia 78, 95123 Catania, Italy
[8] INAF - Osservatorio Astronomico di Trieste, via G.B. Tiepolo 11, 34143 Trieste, Italy

Received 15 September 2011 / Accepted 22 November 2011

ABSTRACT

Context. Several diagnostics ranging from the radio to the X-ray band are suitable for investigating the magnetic activity of late-type stars. Empirical connections between the emission at different wavelengths place constraints on the nature and efficiency of the emission mechanism and the physical conditions in different atmospheric layers. The activity of ultracool dwarfs, at the low-mass end of the main-sequence, is poorly understood.

Aims. We perform a multi-wavelength study of one of the nearest M9 dwarfs, DENIS-P J104814.7-395606 (4 pc), to examine its position within the group of magnetically active ultracool dwarfs, and, in general, advance our understanding of these objects by comparing them to early-M type dwarf stars and the Sun.

Methods. We obtained an *XMM-Newton* observation of DENIS-P J104814.7-395606 and a broad-band spectrum from the ultraviolet to the near-infrared with X-Shooter. From this dataset, we derive the X-ray properties, stellar parameters, kinematics, and the emission-line spectrum tracing chromospheric activity. We integrate these data by compiling the activity parameters of ultracool dwarfs from the literature.

Results. Our deep *XMM-Newton* observation provides the first X-ray detection of DENIS-P J104814.7-395606 ($\log L_x = 25.1$), as well as the first measurement of its V band brightness ($V = 17.35$ mag). The flux-flux relations between X-ray and chromospheric activity indicators are here for the first time extended into the regime of the ultracool dwarfs. The approximate agreement of DENIS-P J104814.7-395606 and other ultracool dwarfs with flux-flux relations for early-M dwarfs suggests that the same heating mechanisms work in the atmospheres of ultracool dwarfs, albeit weaker as judged from their lower fluxes. The observed Balmer decrements of DENIS 1048-3956 are compatible with optically thick plasma in local thermal equilibrium (LTE) at low, nearly photospheric temperature or optically thin LTE plasma at 20 000 K. Describing the decrements with case B recombination requires different emitting regions for Hα and the higher Balmer lines. The high observed Hα/Hβ flux ratio is also poorly fitted by the optically thin models. We derive a similarly high value for the Hα/Hβ ratio of vB 10 and LHS 2065 and conclude that this may be a characteristic of ultracool dwarfs. We add DENIS-P J104814.7-395606 to the list of ultracool dwarfs detected in both the radio and the X-ray band. The Benz-Güdel relation between radio and X-ray luminosity of late-type stars is well-known to be violated by ultracool dwarfs. We speculate on the presence of two types of ultracool dwarfs with distinct radio and X-ray behaviors.

Key words. stars: late-type – X-rays: stars – stars: activity – stars: coronae – stars: individual: DENIS-P J104814.7-395606 – stars: chromospheres

1. Introduction

Late-type stars have long been known to display signatures of magnetic activity that are indicative of solar-like dynamo action (Rosner et al. 1985). Diagnostics of activity are available across the entire electromagnetic spectrum of these stars. The various indicators of magnetic activity probe different layers of the atmosphere. In the radio band, gyrosynchrotron emission from electrons moving in the coronal magnetic field is observed (Güdel 1994). The optical regime is characterized by chromospheric emission lines (Hawley et al. 1996), and the X-ray band displays thermal emission from heated plasma in coronal loops (Schmitt et al. 1995). Strong variability is typical of all radiation originating from magnetic activity, and flares belong to its most obvious manifestations.

In particular, in dM(e) stars ("flare stars") the activity is ubiquitous and flares are more frequently observed than on the Sun. What happens at and beyond the cool end of the main-sequence (spectral types from late-M to L) is less clear. Very low-mass (VLM) stars and brown dwarfs (BDs) are thought to be fully convective and hence a solar-type dynamo is not expected to work. Throughout this paper, we refer to objects with spectral type equal to or later than M7 as ultracool dwarfs (UCDs), regardless of whether they are VLM stars or BDs.

Various optical/infrared emission lines, such as the Balmer series, Ca II H&K, Ca infrared triplet (Ca II IRT), and several

He I lines, trace the chromospheric activity of late-type stars. Empirical relations between the fluxes emitted in these diagnostics yield information about the physical state and origin of the emitting plasma, and their dependence on stellar parameters such as spectral type allow us to unveil how universal the properties of chromospheres are. These flux-flux relations have to our knowledge never been examined for UCDs where Hα emission is usually the only available observable of chromospheric activity.

Surveys of chromospheric Hα activity in UCDs in the solar neighborhood (e.g. Gizis et al. 2000; Reid et al. 2002; Mohanty & Basri 2003; Schmidt et al. 2007) have shown that Hα emission reaches a maximum at spectral type M7, and fades off for the latest M dwarfs. The X-ray regime is widely unexplored beyond spectral type M6. In general, only upper limits to the X-ray luminosity (L_x) are available for a small number of UCDs in the field, and are quite ill-constrained. A possible explanation of the decline in the Hα activity was put forth by Mohanty et al. (2002) who suggested that chromospheric emission might be suppressed because the high electrical resistivity in the cool, neutral atmosphere prevents build-up of substantial magnetic stress. Similar arguments might explain the apparently weak X-ray coronae of UCDs. Direct magnetic field measurements derived from near-infrared (NIR) spectroscopy have demonstrated the presence of kilo-Gauss fields on UCDs (Reiners et al. 2009) but it is unclear at present whether these fields have a structure that is adequate for storing energy. However, UCDs seem to be overluminous in radio by factors of >1000 with respect to the L_R versus (vs.) L_X relation observed for earlier-type active stars (Berger et al. 2005). The detection of radio emission indicates a high-density electron population and the presence of magnetic fields.

A handful of M8 to early-L dwarfs in the solar neighborhood has been found to be the sources of extraordinarily strong Hα, radio, or X-ray emission (for references see Liebert et al. 2003; Berger 2006; Stelzer et al. 2006). In most of these cases, the emission seems to be due to flares. Studies of UCD radio properties have found in some objects a highly circularly polarized pulsed emission component overlaid on their quiescent, non-variable (gyro-synchrotron) emission (e.g. Burgasser & Putman 2005; Hallinan et al. 2006, 2008). The periodicities of the spikes are consistent with the rotational velocities of the objects, implying they originate in a beaming mechanism. This radio component has been attributed to the electron cyclotron maser (ECM) instability, a phenomenon seen in Solar System giant planets rather than in stars.

Seeking to provide additional constraints on the radio/Hα/X-ray connection of UCDs, we observed DENIS-P J104814.7-395606 (henceforth DENIS 1048-3956) with *XMM-Newton*. DENIS 1048-3956 is one of the nearest UCDs (4.00 ± 0.03 pc; Costa et al. 2005). It was classified as an old M9 dwarf because of its lack of lithium absorption (Delfosse et al. 2001). A huge chromospheric flare, identified in a sequence of four high-resolution spectra, was reported by Fuhrmeister & Schmitt (2004). Mass motions related to the flare were inferred from the detection of blueshifts in some emission lines, and interpreted as a rising gas cloud. Radio bursts were observed on DENIS 1048-3956 that are indicative of ECM emission (Burgasser & Putman 2005), but its radio spectrum shows a negative slope typical of gyrosynchrotron emission (Ravi et al. 2011). No X-ray emission could be detected with *ROSAT* (Schmitt & Liefke 2004).

Here we present a deeper X-ray image of DENIS 1048-3956 obtained with *XMM-Newton* and a new broad-band spectrum covering the full optical range and the NIR obtained with X-Shooter at the VLT. The data analysis and results of these two observations are presented in Sects. 2 and 3, respectively. In Sect. 4, we place our findings in the context of magnetic activity on other UCDs and earlier-type M dwarfs. We present for the first time flux-flux relations between chromospheric and coronal radiation involving UCDs. We compare the observed Balmer decrements of DENIS 1048-3956 to those of other late-type dwarf stars and to theoretical predictions from which we obtain clues about the physical conditions of the emitting region. Finally, we discuss the connection between the radio and X-ray emission of UCDs, including the new data for DENIS 1048-3956. All this is achieved by making use of an updated compilation of the X-ray, Hα and radio properties of UCDs. We also analyzed archived and as yet unpublished X-ray data for two UCDs, DENIS-P J1228.2-1547 (henceforth abbreviated DENIS 1228-1547) and PC 0025+0447. A summary of our results and conclusions is given in Sect. 5.

2. *XMM-Newton* data analysis

DENIS 1048-3956 was observed by *XMM-Newton* for 20 ks on Jan. 17, 2010 (Obs-ID 0600410101). *XMM-Newton* acquired both X-ray and optical data for DENIS 1048-3956 using EPIC and the Optical Monitor (OM). These data were analysed with Standard *XMM-Newton* Science Analysis System (SAS) software (v9.0).

2.1. X-ray data

This data analysis closely follows the procedure that was described in detail by Barrado et al. (2011), and we briefly summarize here the individual steps. We first created photon event lists with the metatasks EPCHAIN and EMCHAIN for EPIC/pn and EPIC/MOS, respectively. After standard data filtering, we performed source detection for each of the three detectors. DENIS 1048-3956 is detected as a weak X-ray source on EPIC/pn but not on the two MOS detectors. Most of the photons detected in EPIC/pn have energies <2 keV. Therefore, to maximize the sensitivity, in a second step we merged the data of all three instruments and then repeated the source detection procedure on the merged data for energies between 0.2 keV and 2.0 keV. Taking account of the different relative sensitivity of EPIC/pn and EPIC/MOS by scaling the exposure maps of EPIC/pn accordingly, the resulting combined data set has an effective EPIC/MOS exposure of 101 ks at the position of DENIS 1048-3956. We then repeated the source detection procedure on the merged data, and found a source count rate of $(1.16 \pm 0.14)\ 10^{-3}$ cts/s for DENIS 1048-3956.

Owing to the low photon statistics, we attempted no spectral analysis and assumed a plasma temperature between 0.6...1.0 keV to estimate the flux with the help of PIMMS[1]. This yields an intrinsic X-ray luminosity of $\log L_x\,[\mathrm{erg/s}] = 25.1$ with practically no dependence on the temperature within the assumed range. Our measurement is consistent with the upper limit measured from *ROSAT* data ($\log L_x\,[\mathrm{erg/s}] < 26.3$; Schmitt & Liefke 2004). Fuhrmeister & Schmitt (2004) give a bolometric luminosity of 1.5×10^{30} erg/s using $d = 4.6$ pc. Correcting this value for our updated distance estimate, the fractional X-ray luminosity of DENIS 1048-3956 is $\log (L_x/L_{bol}) = -5.0$.

We extracted a lightcurve for DENIS 1048-3956 and searched for variability with a maximum likelihood (ML) method that divides the sequence of photons into intervals of

[1] The Portable Interactive Multi-Mission Simulator is available at http://cxc.harvard.edu/toolkit/pimms.jsp

Table 1. Summary of OM observations and results for DENIS 1048-3956.

	Exposure number				
	006	007	008	009	011
Date-Obs [JD-2 455 214]	0.025463	0.067014	0.107639	0.184028	0.221065
Expo [s]	4400	4380	4200	3000	2200
α_{2000} [hh:mm:ss.ss]	10:48:13.57	10:48:13.58	10:48:13.58	10:48:13.56	10:48:13.55
δ_{2000} [dd:mm:ss.ss]	−39:56:16.87	−39:56:16.85	−39:56:16.90	−39:56:16.82	−39:56:16.89
$V_{\rm ins}$ [mag]	17.32 ± 0.03	17.26 ± 0.03	17.37 ± 0.03	17.42 ± 0.04	17.40 ± 0.04

constant signal and subtracts the background from the photon time series on a statistical basis (see Stelzer et al. 2007). Two short and weak flare-like intensity enhancements are seen in the binned lightcurve. Only one of these events is recognized by the ML algorithm at 95% significance.

2.2. Optical data

During the X-ray observation, the Optical Monitor (OM) operated in the Fast Mode with the V band filter. The central Fast Mode window was used with a time-resolution of 10 s. A larger image window recorded contemporaneously with the Fast Mode data an image of the region around DENIS 1048-3956. The maximum allowed exposure time for the chosen Fast Mode setup is 4400 ks. Therefore, the OM observation was divided into five consecutive exposures (see Table 1). The OM data was processed with standard SAS procedures.

There is no obvious variability in the 10 s-binned lightcurves. However, a comparison of the average brightness levels of the five exposures shows small variations with a minimum count rate of 1.45 ± 0.05 cts/s and a maximum count rate of 1.65 ± 0.04 cts/s for DENIS 1048-3956, i.e. variations at a 2σ level on timescales of a few hours.

The time-averaged instrumental magnitude of DENIS 1048-3956 derived from the Fast Mode data is $V_{\rm ins}$ = 17.35 ± 0.02 mag. This number cannot be converted into standard magnitude with the SAS procedures because observations were performed in a single filter and, consequently, no color information is available. We estimated the conversion factor from instrumental to standard $V_{\rm std}$ band magnitude using our previous experience with the OM. In our survey of the young cluster Collinder 69 (Barrado et al. 2011), B and V band exposures were obtained and the (standard) $B-V$ derived for the objects in this field covers a wide range. For an M8 dwarf, the expected[2] $B-V$ is 2.2 mag, and for this value we found from the parabolic relation between $V_{\rm ins} - V_{\rm std}$ and $(B-V)_{\rm std}$ for Collinder 69 a correction factor of 0.11 mag, i.e. $V_{\rm std}$ = 17.24 mag. Combining this with the B band measurement of DENIS 1048-3956 from the literature, we obtained $B-V$ = 1.76 mag, which is much smaller than the assumed value. While this difference may be due to the intrinsic source variability of the non-contemporaneous data, there are no strong constraints on the blue colors of late-M dwarfs. When we assumed the lower value for $B-V$ that we derived above, the filter transformation factor reduced to 0.075 mag, and $V_{\rm std}$ = 17.28 mag. Further iteration did not yield significant changes. Therefore, we adopted an uncertainty of ±0.04 mag and a value of $V_{\rm std}$ = 17.35 ± 0.04 mag.

The Image Mode data do not yield additional brightness information but they can be used for a comparison of the present-day position of DENIS 1048-3956 with its position expected from its proper motion given in the literature. A boresight correction needs to be applied to take account of small OM pointing errors. The OM images have artifacts such as ghosts. In principle, the $Q_{\rm FLAG}$ in the source list may be used to identify reliable sources. However, Kuntz et al. (2008) demonstrated that the *SIGNIF* parameter is a more robust indicator of the reality of a source than $Q_{\rm FLAG}$. We selected by visual inspection a number of optical sources with 2 MASS counterparts distributed across the OM image but avoided areas with obvious artifacts. We then cross-correlated the positions of the selected objects in the two catalogs and searched iteratively for the mean offset in α and δ. The results were $\Delta\alpha = -0.06''$ and $\Delta\delta = -1.71''$ for Expo. No. 006. These values are in the range cited by Talavera (2009) for the typical OM pointing accuracy.

3. X-Shooter data analysis

DENIS 1048-3956 was observed on Apr 06, 2010 with the X-Shooter spectrograph at the VLT (ESO; Chile). The data were acquired within the INAF/GTO time (Alcalá et al. 2011). With its three spectrograph arms, X-Shooter provides simultaneous wavelength coverage in the spectral range 3000–24 800 Å. Slit widths of 0.5″/0.4″/0.4″ were used in the UVB/VIS/NIR arms, respectively, yielding spectral resolutions of 9100/17400/11300. The total exposure time in each of the three spectrograph arms was 1200 sec. The data were obtained in the so-called *nod* mode and were reduced independently for each arm with the X-Shooter pipeline v1.0.0 (Modigliani et al. 2010), following the standard steps: bias or dark subtraction, flat fielding, optimal extraction, wavelength calibration, and sky subtraction. The final outcome of this procedure is a one-dimensional spectrum that we flux-calibrated using a standard star observed during the same night and corrected for atmospheric extinction with our own IDL[3] routines.

The flux-calibrated spectrum of all three arms is shown in Fig. 1. At the conjunction of two arms (UVB/VIS and VIS/NIR), the match of the flux scale is excellent. Photometry from the literature[4] is superimposed, providing further evidence of the high quality of the flux calibration. We note in particular the very good agreement of our V band measurement from the *XMM-Newton* OM with the X-Shooter spectrum. A discrepancy of roughly a factor of two between the photometry and the X-Shooter spectrum is present in the NIR, possibly owing to residual problems with the flux calibration of the NIR spectrum. We note, however the good match of the NIR and the VIS spectrum. We do not know the origin of the offset between the NIR spectrum and photometry but do not place much weight

[2] http://www.pas.rochester.edu/~emamajek/memo_M.html

[3] The Interactive Data Language (IDL) is a trademark of ITT Visual Information Systems.

[4] The $BRi_{\rm D}JK_{\rm S}$ magnitudes are from Delfosse et al. (2001), $JHK_{\rm s}$ magnitude from 2 MASS and the V magnitude from our measurement with the *XMM-Newton* OM presented in Sect. 2. The B and R photometry has been converted from USNO to the standard system using the equations given on http://www.britastro.org/asteroids/USNO%20photometry.htm

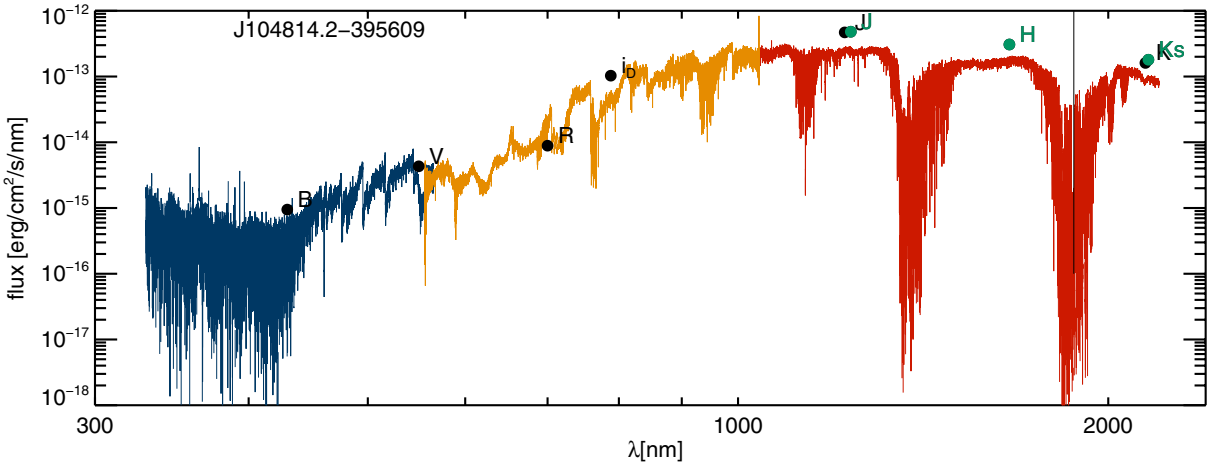

Fig. 1. Broad-band flux-calibrated X-Shooter spectrum of DENIS 1048-3956. The spectra from the three X-Shooter arms are shown in different colors. Published photometry from the literature is overplotted. The 2 MASS JHK_S magnitudes are shown with a slightly different color to distinguish them from the DENIS JK_S photometry given by Delfosse et al. (2001). At the blue end, the spectrum is dominated by noise caused by the intrinsic faintness of DENIS 1048-3956. Telluric absorptions are clearly visible especially in the NIR spectrum.

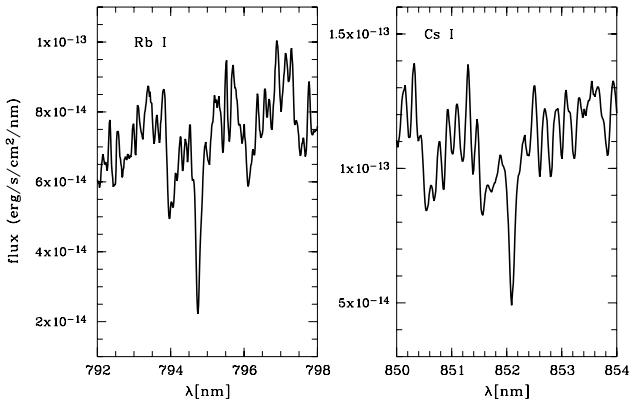

Fig. 2. Detail of the spectrum of DENIS 1048-3956 in the wavelength range around the Rb I and Cs I absorption lines.

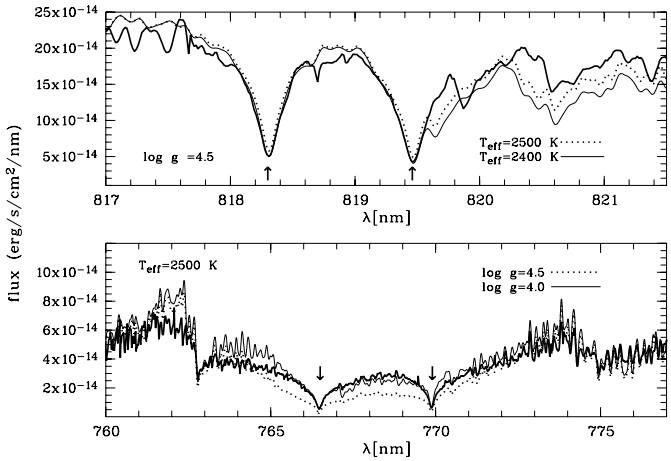

Fig. 3. Detail of the spectrum of DENIS 1048-3956 (thick solid lines) in the wavelength range around the Na I (*upper panel*) and K I (*lower panel*) absorption doublets. The spectrum of DENIS 1048-3956 has been corrected for telluric absorption lines. The dotted line and the thin solid line represent synthetic spectra with $T_{\rm eff}$ and $\log g$ as labelled.

on it because, in practice, our data analysis concentrates on the UVB and VIS spectra.

The spectrum of the VIS arm (550–1050 nm), properly corrected for the telluric absorption, was used to estimate several astrophysical parameters, such as spectral type, effective temperature ($T_{\rm eff}$), gravity ($\log g$), and radial velocity (RV), as we describe in Sects. 3.1 and 3.2. The spectra of all three arms were searched for emission lines for which we measured the equivalent width (EW) and flux ($f_{\rm line}$), as outlined in Sect. 3.3.

3.1. Fundamental stellar parameters

As shown by Basri et al. (2000), the Rb I at λ 794.76 nm and Cs I at λ 852.11 nm absorption lines are very sensitive to the effective temperature of VLM stars and BDs. These two lines are very clearly detected in our X-Shooter spectrum (see Fig. 2). We measured equivalent widths of 0.09 ± 0.01 nm and 0.06 ± 0.01 nm for Rb I and Cs I, respectively. These values correspond to a temperature of ≈2450 K according to the temperature scale of Basri et al. (2000), which is consistent with a spectral type M9 and agrees with previous values for the spectral type (e.g. Reiners & Basri 2010). We obtained an independent estimate of the spectral type using the spectral index PC 3 defined by Martín et al. (1999c) and found a spectral type of M8.8 that matches our above results.

To derive other physical parameters, we used synthetic model spectra gathered from the *star, brown dwarf & planet atmosphere web simulator* (Allard et al. 2010), electronically available[5]. A grid of synthetic spectra was generated in the parameter space 2300 K < $T_{\rm eff}$ < 2600 K and 4.0 < $\log g$ < 4.5, in steps of 100 K and 0.5 dex in $T_{\rm eff}$ and $\log g$, respectively, while keeping $v \sin i = 0$ km s^{-1} and solar metallicity fixed. The literature values for the rotational velocity of DENIS 1048-3956 were around 20 km s^{-1} but at the resolution of the X-Shooter spectrum we are insensitive to this parameter, as discussed in Sect. 3.2.

In low-mass stars and BDs, the Na I doublet at $\lambda\lambda$ 818.33, 819.48 nm is very sensitive to both $T_{\rm eff}$ and $\log g$. These lines were used to estimate temperature and gravity. We found a close match between observed and synthetic spectra for $T_{\rm eff}$ = 2450 ± 100 K and $\log g$ = 4.5 ± 0.5 dex (see Fig. 3). The temperature is in good agreement with the value derived from the equivalent width of the Rb I and Cs I lines above. Fitting the K I absorption doublet at $\lambda\lambda$ 766.48, 769.89 nm inferred a

[5] http://phoenix.ens-lyon.fr/simulator/index.faces

similar temperature, but the only way to obtain a reasonable fit to the wings of the lines was to use a synthetic spectrum with a lower gravity. This is shown in the bottom panel of Fig. 3, where the two synthetic models with $\log g = 4.0$ and $\log g = 4.5$ but the same $T_{\rm eff} = 2500$ K are overplotted on the X-Shooter spectrum. A similar result is obtained when using the Na I doublet at $\lambda\lambda$ 588.99, 589.59 nm, although the signal-to-noise ratio of the X-Shooter spectrum in this wavelength range is quite low (∼7). From the above results, we concluded that reliable values for the temperature and gravity of DENIS 1048-3956 are $T_{\rm eff} = 2450 \pm 50$ K and $\log g = 4.3 \pm 0.3$, respectively.

3.2. Rotation and kinematics

Literature values for the $v \sin i$ of DENIS 1048-3956 have been reported to range from 18 to 30 km s^{-1} (Delfosse et al. 2001; Fuhrmeister & Schmitt 2004; Reiners & Basri 2009). These determinations are based on spectra with a much higher resolution than our X-Shooter spectrum. Including $v \sin i$ as a parameter in our fits does not change the results for the stellar parameters. We have cross-correlated the VIS X-Shooter spectrum, corrected for telluric contribution, with a synthetic spectrum with zero rotation. The synthetic spectrum was retrieved from the web simulator of Allard et al. (2010) by matching both the resolution and astrophysical parameters of DENIS 1048-3956. The cross-correlation function had an apparently broad but well-detected peak. The width decreased when strong molecular bands were not considered in the cross-correlation. We measured a width of 20–30 km s^{-1} depending on the placement of the cross-correlation background. Thus, a reasonable value of $v \sin i$ from the X-Shooter spectrum is 25 ± 5 km s^{-1}, in agreement with previous measurements.

We estimated the RV of DENIS 1048-39 by measuring the Doppler shift of several Na I absorption lines. The result, after applying the corresponding barycentric correction (−4.6 km s^{-1}) was RV = −11.4 ± 2.0 km s^{-1}. This result is in agreement with previous RV determinations (Montes et al. 2001). Using our radial velocity estimate and the proper motion components of the star, $\mu_\alpha \cos\delta = -1178.4 \pm 12.7$ mas yr^{-1}, $\mu_\delta = -986.4 \pm 12.7$ mas yr^{-1}, retrieved from the PPMXL Catalog (Roeser et al. 2010), we derived spatial velocity components of the star adopting the distance $d = 4$ pc. The results, corrected for solar motion (Schönrich et al. 2010) in a left-handed coordinate system, are $(U, V, W) = (+0.26 \pm 0.071, +13.6 \pm 1.9, -21.9 \pm 1.1)$ km s^{-1}, where U, V, and W are directed towards the Galactic anti-center, the Galactic rotation direction, and the North Galactic Pole, respectively. These velocity components indicate that DENIS 1048-3956 is kinematically consistent with those of the galactic young disk population. We note that Montes et al. (2001) reached a similar conclusion. We stress that these results are in line with the $\log g$ value derived for DENIS 1048-3956 in Sect. 3.1.

3.3. Emission line spectrum

During the X-Shooter observation, DENIS 1048-3956 displayed a weak emission-line spectrum resulting from chromospheric activity. We detected the Balmer series up to H8. The Hϵ line can be clearly distinguished from Ca II H. While the Ca II H&K lines are in emission, the Ca II IRT is not detected, and no NIR emission lines are seen. The Na I doublet at $\lambda\lambda$ 588.99, 589.59 nm is in absorption with central emission peaks in both lines. In this case, deriving the chromospheric losses requires the subtraction of the photospheric absorption profile. We used the "spectral synthesis" technique, based on the comparison between the target spectrum and the best-fit synthetic spectrum ($T_{\rm eff} = 2500$ K and $\log g = 4.0$), that we used as a "reference spectrum" to account for the non-active photospheric emission. The difference between the observed and the reference spectrum provides, as a residual, the net chromospheric line emission, which can be integrated to find the total radiative losses in the line (see, e.g., Frasca & Catalano 1994).

Table 2. Emission line parameters for DENIS 1048-3956.

Line	$\lambda_{\rm line}$ [nm]	$EW_{\rm line}$ [nm]	$\log f_{\rm line}$ [erg/cm^2/s]
Ca K	393.356	$-1.76^{-4.74}_{+0.98}$	$-15.72^{+0.03}_{-0.02}$
Ca H	396.833	$-1.19^{-6.67}_{+0.76}$	$-15.86^{+0.03}_{-0.05}$
H8	388.893	$-0.12^{-0.17}_{+0.06}$	$-16.71^{+0.06}_{-0.11}$
Hϵ	396.995	$-0.19^{-0.44}_{+0.11}$	$-16.56^{+0.14}_{-0.14}$
Hδ	410.159	$-0.19^{-0.34}_{+0.09}$	$-16.49^{+0.06}_{-0.09}$
Hγ	434.035	$-0.19^{-0.13}_{+0.07}$	$-16.13^{+0.07}_{-0.09}$
Hβ	486.110	$-0.13^{-0.02}_{+0.02}$	$-15.80^{+0.03}_{-0.05}$
Na I D1	589.577	$-0.07^{-0.01}_{+0.01}$	$-15.94^{+0.10}_{-0.14}$
Na I D2	588.980	$-0.03^{-0.01}_{+0.01}$	$-15.61^{+0.05}_{-0.07}$
Hα	656.240	$-0.07^{-0.03}_{+0.03}$	$-14.94^{+0.14}_{-0.25}$

We applied this technique to the Hα and the Na I D lines while for the other emission lines it was unnecessary because the photospheric contribution in absorption is negligible. In Fig. 4 left, we show the spectrum of DENIS 1048-3956 in the Hα and Na I regions, together with the reference synthetic spectrum, which is representative of the star in the absence of chromospheric activity. The Hα profile is clearly in emission, while the Na I lines are in absorption with an emission core. The residual equivalent width of the lines was measured by integrating the full emission profile in the subtracted spectrum (see right panel of Fig. 4). The error in the EW (σ_{EW}) was evaluated by multiplying the integration range by the photometric error in each point. The latter was estimated to be the standard deviation of the observed fluxes in the difference spectra for the two spectral regions near the line. The final line-residual equivalent widths and line fluxes for Na D and Hα are given in Table 2 together with those of all other emission lines. Note, that no helium lines are detected (e.g. He I D_3 587.6 nm), although these lines are often detected in the spectra of flare stars. For all lines in Table 2 except for Na D and Hα, we obtained the line flux by directly integrating the line profile in the observed spectrum. The uncertainties were determined from the local fluctuation of the continuum.

A parameter of particular relevance to this study of multi-wavelength activity is $\log(L_{\rm H\alpha}/L_{\rm bol})$. Taking account of the distance, the observed Hα flux corresponds to $L_{\rm H\alpha} = (3.8 \pm 0.8) \times 10^{24}$ erg s^{-1}. An alternative means of computing line luminosities involves the surface flux and radius of the star. To derive the luminosity of a given line from the equivalent width, the surface flux of the continuum ($F^{\rm C}_\lambda$) must be known. We inferred the stellar radius from the COND03 models (Baraffe et al. 2003) that most closely matched the temperature and gravity, while $F^{\rm C}_\lambda$ was estimated from the flux-calibrated synthetic spectrum of the same $T_{\rm eff}$ and $\log g$. In this way, we found that $R_* = 0.13\,R_\odot$ and $F^{\rm C}_{\rm H\alpha} \sim 8.5 \times 10^4$ erg/cm^2/s/nm. The resulting line luminosity is $L_{\rm H\alpha} = (6.3 \pm 2.6) \times 10^{24}$ erg/s, which agrees within the uncertainties with the value derived from the integrated line flux. We computed the $L_{\rm H\alpha}/L_{\rm bol}$ value from the mean of the

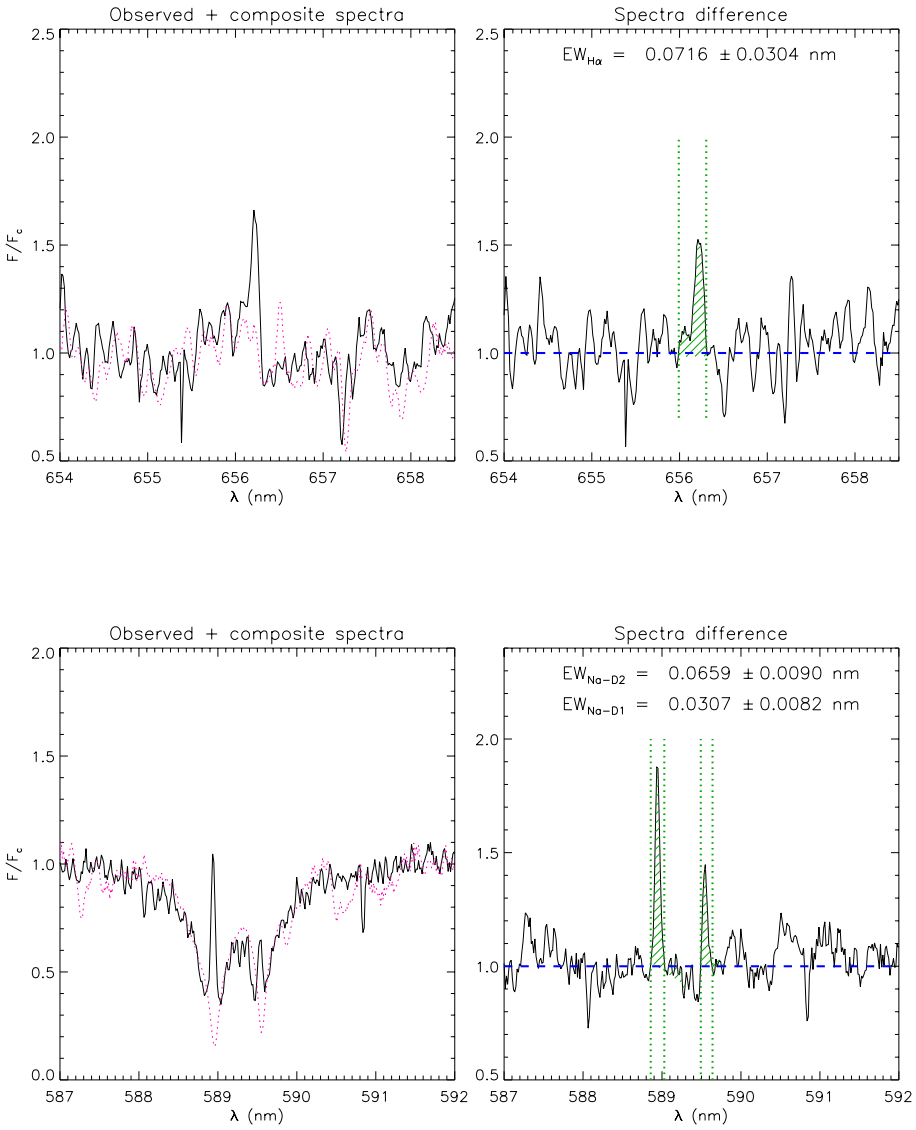

Fig. 4. *Left panels*: observed, continuum-normalized X-Shooter spectrum of DENIS 1048-3956 (solid line) in the Hα and Na I D regions (*top and bottom*, respectively), together with the synthetic template (dotted line). *Right panels*: difference between the observed and template spectra. The hatched areas represent the excess emissions that were integrated to derive the net equivalent width.

Hα luminosities computed with the two methods, and obtained $\log(L_{H\alpha}/L_{bol}) = -5.3$. This is similar to the value presented by Schmidt et al. (2007) ($\log(L_{H\alpha}/L_{bol}) = -5.2$) but much lower than the measurement of Fuhrmeister & Schmitt (2004) during a large flare ($\log(L_{H\alpha}/L_{bol}) = -4.0$).

4. Multi-wavelength picture of activity on UCDs

To understand more clearly the nature of DENIS 1048-3956, we now compare its multi-wavelength properties to those of earlier M dwarfs and other UCDs. For this purpose, we compiled a list with activity diagnostics for UCDs comprising X-ray, Hα, and radio luminosities, rotational velocity, and magnetic field strength.

4.1. Flux-flux relations

The relative radiative losses in different parts of the chromosphere and the corona can be quantified by relations between the radiation emitted in different lines. The connection between various chromospheric lines and soft X-ray emission has been shown for various samples of late-type main-sequence stars to result in power-law relations between the fluxes, i.e. linear relations in log-log form of the type $\log F_1 = c_1 + c_2 \times \log F_2$, where c_2 is the power-law slope and F_1 and F_2 are the surface fluxes of the two diagnostics. Observational results and also their interpretation have been ambiguous if not contradictory. In early studies, a spectral-type dependence of the slopes has repeatedly been found in comparisons of X-ray flux to chromospheric fluxes (Hα, Ca II H+K) with M dwarfs having a shallower slope than G dwarfs. These differences have been attributed to either an excess of chromospheric emission in M dwarfs (e.g. Schrijver & Rutten 1987; Rutten et al. 1989) or a deficiency of coronal emission in G dwarfs (Doyle 1989). However, the lack of simultaneity in the observations and the use of different techniques to determine chromospheric fluxes by distinct authors mean that this hypothesis may not be applicable. Martínez-Arnáiz et al. (2011a, henceforth referred to as MA11) found that all the main-sequence dwarf stars seem to follow the same relation between the surface flux in X-rays and Hα, while differences are found for very active K and M dwarfs when comparing X-rays with Ca II lines.

Schrijver et al. (1989) ascribed the minimum flux level observed for a given spectral type in chromospheric and transition region emissions to a "basal" chromospheric flux that is due to non-magnetic heating of the outer atmosphere and needs to be subtracted when investigating flux-flux relations to probe magnetic activity. Indeed, only when the "basal" chromospheric flux

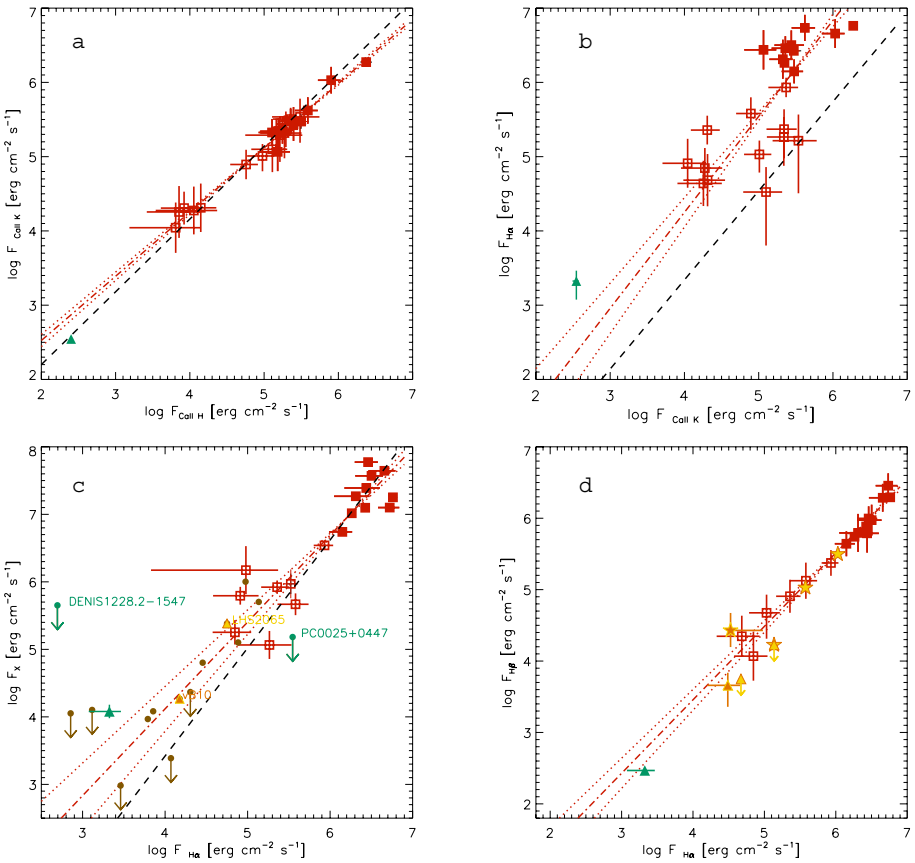

Fig. 5. Relations between chromospheric and coronal activity diagnostics for the sample of M dwarfs from MA11 (red) with linear regression fits (red dash-dotted) and their variance (red dotted) and for comparison the fits derived by Martínez-Arnáiz et al. (2011b) for their whole sample of F-M dwarfs (black dashed): **a)** Ca II K vs. Ca II H flux; **b)** Hα vs. Ca II K flux; **c)** X-ray vs. Hα flux; and **d)** Hβ vs. Hα flux. Also plotted, but not included in the fits, in all panels is DENIS 1048-3956 (green triangle), in panel **c)** UCDs from the literature (brown circles, orange and yellow triangles) and two UCDs for which we present new X-ray data (PC 0025+0447 and DENIS 1228-1547; green circles), and in panel **d)** two UCDs with both Hα and Hβ measurements from the literature (vB 10 in orange and LHS 2065 in yellow; triangles represent quiescence, and star symbols the flare state; the data points for LHS 2065 correspond to four consecutive spectra tracking the decay of a large flare and show that in the course of the flare evolution, its Hα and Hβ fluxes vary along the flux-flux relationship for earlier M dwarfs).

is subtracted can clear relations be found. We refer the interested reader to Sects. 3.1 and 5.1 of MA11 for a complete description of techniques, previous works and results on this issue.

MA11 have presented flux-flux relations combining a sample of nearly 300 single dwarf stars with spectral types from F to mid-M. Given the above caveats, it seems in order to examine flux-flux relations for stars of different spectral type separately. We examine here for the first time chromospheric and coronal flux-flux relations for UCDs by comparing DENIS 1048-3956 to the subsample of M dwarfs from MA11. The sample of MA11 comprised 39 single dwarf stars with spectral types from M0 to M5. MA11 identified two groups of M dwarfs. The 'inactive' M dwarfs follow the same relationships between Hα and various calcium lines (Ca II H&K, Ca II IRT) as those derived for the stars with earlier spectral type in the MA11 sample. The "active" M dwarfs display an excess of Hα flux with respect to these relations. The "active" and "inactive" groups are distinguished by the former ones being saturated in terms of L_X/L_{bol} and being younger than the average.

MA11 derived power-law relations between calcium lines, Hα, and L_x for their total stellar sample. Here, we take into consideration only their M dwarfs and extend the study to the remaining Balmer lines. Equivalent widths for Hα to Hϵ were measured from the spectra presented by MA11 (see López-Santiago et al. 2010, for a detailed description of the process) but have not been published so far. To obtain the surface fluxes for the MA11 sample, we used the χ factors given by West & Hawley (2008). The χ factor is defined as $\chi_i = f_{cont,i}/f_{bol}$, where $f_{cont,i}$ is the continuum flux near a certain emission line i and f_{bol} the bolometric flux. West & Hawley (2008) calibrated χ_i as a function of spectral subclass for M0 to L0 from a sample of nearby dwarfs with flux-calibrated spectra. Multiplying χ_i with the observed line equivalent width yields the fractional line flux, $f_{line,i}/f_{bol}$, which is equivalent to the fractional line luminosity, $L_{line,i}/L_{bol}$. We obtained the individual bolometric luminosity and the stellar radii required to convert luminosity to surface flux from the models by Siess et al. (2000) assuming that all stars from the MA11 sample are on the zero-age main-sequence.

As a result of the low spectral resolution of the SDSS spectra, West & Hawley (2008) presented a joint χ value for Ca II H+K and Hϵ, while these three lines are resolved in the M dwarf sample from MA11. Given the negligible variation in the continuum flux across the short wavelength range comprising these three lines, the same χ factor can be used to derive individual line fluxes for Ca II H, Ca II K, and Hϵ.

In Fig. 5, we reproduce some of the plots from MA11 including only their M stars. We examined only those relations for which we had measured data for DENIS 1048-3956, i.e. the study of the Ca II IRT was excluded. The flux for the Ca II IRT line at λ8498 Å predicted for DENIS 1048-3956 from the flux-flux relation of Ca II K vs. Ca II IRT λ8498 from MA 11 is 1.7×10^{-16} erg/cm^2/s. This is within the noise level in the X-Shooter spectrum meaning that its non-detection is plausible. We note that MA11 derived surface fluxes from empirical relationships between continuum flux at the line position and $B-V$ color following Hall (1996). Therefore, there are slight differences between their fluxes and those that we derived with the χ-factors. However, MA11 showed in their Fig. 2 that there is a very good correlation between the results of both methods. For DENIS 1048-3956, we prefer the fluxes obtained directly from the flux-calibrated spectrum with respect to those calculated from χ-factors because the former ones have much smaller uncertainties and are available for a larger number of lines.

The error bars in Fig. 5 reflect the uncertainties in the measurement of the line equivalent width and the χ-factors, and are

Table 3. Linear fit coefficients of flux-flux relationships for the M dwarfs from MA11.

Line 1	Line 2	N_*	c_1	c_2
Ca K	Ca H	24	0.82 ± 0.46	0.86 ± 0.08
Hα	Ca K	22	-1.32 ± 0.85	1.26 ± 0.15
X-rays	Hα	18	-1.02 ± 0.94	1.29 ± 0.15
Hα	Hβ	16	-0.66 ± 0.41	1.03 ± 0.07
Hα	Hγ	14	-1.33 ± 0.32	1.06 ± 0.05
Hα	Hδ	13	-2.36 ± 0.47	1.20 ± 0.08
Hα	Hϵ	10	-14.66 ± 5.63	2.96 ± 0.87
Hβ	Hγ	14	-0.94 ± 0.18	1.08 ± 0.03
Hβ	Hδ	13	-1.40 ± 0.14	1.14 ± 0.03

Notes. Linear regression fits are of the type $\log F_1 = c_1 + c_2 \times \log F_2$ and Col. 3 gives the number of stars in the sample.

dominated by the latter. Additional errors in the assumption of the individual radii and distances are not taken into account. Stars from MA11 with multiple observations are plotted at the mean of the measured flux with an error bar that represents the standard deviation in the individual measurements. The "active" group defined by MA11 is recognizable as filled squares.

We performed linear regression fits to this subsample of M dwarfs (dash-dotted lines in Fig. 5), which can be compared to the linear regressions derived by MA11 and corrected by Martínez-Arnáiz et al. (2011b) for the whole sample of F-M dwarfs (dashed lines). In Table 3, we give the values obtained for our linear regressions, including Balmer lines that were not included in MA11 and for which data were measured but not published before. We note that we carried out the fitting process using different techniques described by Isobe et al. (1990). We report in Fig. 5 and in Table 3 the results from the least squares bisector regression, a method that is adequate in cases where the intrinsic scatter in the data dominates over the measurement errors and that treats the X and Y variables symmetrically. The same technique was used by MA11 and Martínez-Arnáiz et al. (2011b), making the results directly comparable. Our power-law slope of $F_{\rm Ca\,K}$ vs. $F_{\rm Ca\,H}$ agrees well with that derived by Martínez-Arnáiz et al. (2011b), while that of $F_{\rm H\alpha}$ vs. $F_{\rm Ca\,K}$ and of $F_{\rm x}$ vs. $F_{\rm H\alpha}$ are slightly different from the results of Martínez-Arnáiz et al. (2011b) considering the 1 σ uncertainties. DENIS 1048-3956 is shown as a green triangle in all plots and is not included in the fitting process (nor are any of the other UCDs that are shown in some of the plots as described below).

First, we concentrate on some features in the derived flux-flux relations. While the Ca II H and Ca II K lines show a tight correlation, the plot of Hα vs. Ca II K flux displays a very large scatter. Rather than a clear relation, there seem to be two separate clouds of data for the "active" and the "inactive" stars. We note, that the scatter in this plot becomes even larger if stars of spectral types F-K are included. This is also the reason for the vertical offset in our linear regression with respect to the results of Martínez-Arnáiz et al. (2011b) in Fig. 5b. Indeed, MA11 defined their "active" and "inactive" sample on the basis of this plot. X-ray vs. Hα flux shows a much clearer correlation, although this plot also shows considerable scatter. As an example of the flux-flux relations between Balmer lines, which are presented here for the first time for the MA11 sample, in Fig. 5d Hβ vs. Hα is displayed. Very tight correlations are observed for all combinations of Balmer line fluxes (see Table 3 for the results of the regression analysis).

In Fig. 5c and 5d, we include data on UCDs compiled from the literature. To obtain the individual surface fluxes for the lines from the published equivalent widths, we assumed radii between 0.12 and 0.16 $R_\odot$ depending on the spectral type, in accordance with the predictions of the Baraffe et al. (2003) model atmospheres for high-gravity ($\log g = 4.5$) M7-L0 dwarfs. When more than one epoch of X-ray or Hα data was available for these objects we assumed that the minimum measured value is representative of the quiescent emission. This is justified because the spectra of M dwarfs from MA11 from which the flux-flux relations are derived represent snapshots for individual stars and this sample is, therefore, unlikely to be dominated by flares[6]. Analogously, the position of DENIS 1048-3956 in Fig. 5 represents its lowest observed coronal and chromospheric flux, i.e. the calcium and Balmer line fluxes from our X-Shooter spectrum and our new *XMM-Newton* detection.

Compared to the extrapolation of the flux-flux relations to low fluxes, DENIS 1048-3956 displays several deviations. In the relation between Hα and Ca II K flux, DENIS 1048-3956 has an excess of Hα for its Ca II emission and in terms of Ca II K vs. Ca II H it is also outside by $>3\sigma$ of the very tight relation. In the X-ray vs. Hα flux plot, DENIS 1048-3956 is marginally compatible with the relation derived for the MA11 sample. As for DENIS 1048-3956, most of the other UCDs agree well with the extension of the X-ray/Hα relation of early-M dwarfs to lower fluxes. We mention in passing that the analysis of the UCDs did not comprise the spectral subtraction technique and, in principle, all line fluxes may be underestimated. However, from our experience with DENIS 1048-3956 we do not expect this to be a notable effect. Two UCDs (PC 0025+0447 and DENIS 1228-1547) for which we present new X-ray data in the appendix are highlighted by green circles. The deviation of PC 0025+0447 from the X-ray/Hα correlation is due to its notoriously bright Hα emission (Schneider et al. 1991). Two UCDs (LHS 2065 and vB 10) for which we discuss below the Balmer decrements are also highlighted in different colors. Further UCDs with detected Hα emission beyond the lower end of the flux range shown in Fig. 5c have meaninglessly high upper limits in X-rays.

4.2. H I line ratios

Ratios of line fluxes are often used for flare stars to characterize the emitting plasma. We compared the Balmer decrements of DENIS 1048-3956 to those measured for other M dwarfs and the Sun (Sect. 4.2.1) and to the theoretical values predicted for different assumptions about the physical conditions of the emitting gas (Sect. 4.2.2).

4.2.1. Observed Balmer decrements

The Balmer decrements are here referred with respect to Hβ. We computed the available Balmer flux ratios for the M dwarf sample from MA 11 and for DENIS 1048-3956. In addition, we computed fluxes for the Hα and Hβ emission of two UCDs

[6] The range of observed Hα fluxes for the individual objects in our UCD sample is between 0.5 and 2 dex. This is larger than the typical short-term Hα variations (of a factor of two in $\Delta t \leq 1$ h) observed on M dwarfs (e.g. Crespo-Chacón et al. 2006; Lee et al. 2010; Kruse et al. 2010). These differences are probably due to the much shorter timescales examined in these latter studies and observational biases in our sample in favor of UCDs that have caught attention because of their flaring activity either in Hα or X-rays. Similarly, the majority of UCDs with an X-ray detection displayed an X-ray flare, and, therefore, the mean of the *observed* fluxes is biased towards high values making the lowest observed flux a more robust measure for the typical emission level.

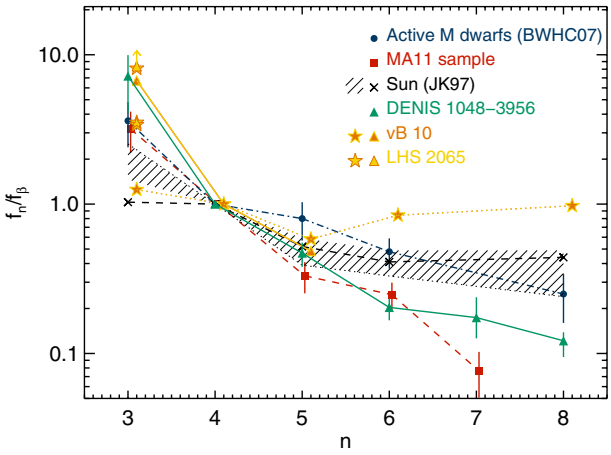

Fig. 6. Balmer decrements for DENIS 1048-3956 compared to the M dwarf sample from MA11, the active M dwarf templates from Bochanski et al. (2007), the Sun from Johns-Krull et al. (1997), and the UCDs vB 10 (Berger et al. 2008) and LHS 2065 (Martín & Ardila 2001). The latter two objects are plotted with a small horizontal offset for clarity, and we distinguish their flare phase (star symbols) from the quiescent state. Similarly, for the Sun the range observed during a large flare is shown as a shaded area where the late flare phase is highlighted by a thin dotted line, while the quiet Sun decrements are connected by a dashed line.

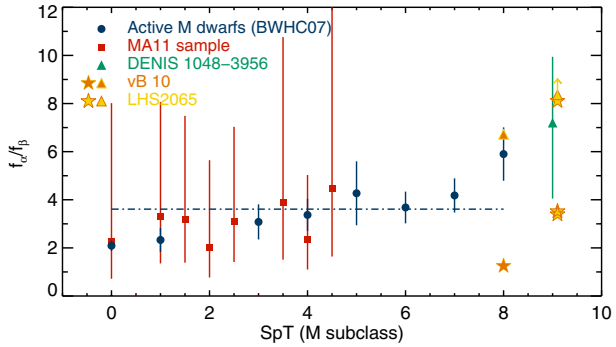

Fig. 7. Hα/Hβ flux ratio as a function of spectral type for M dwarfs. Same plotting symbols as in Fig. 6. The dash-dotted line denotes the mean over all spectral types for the BWHC07 sample.

from the equivalent widths given in the literature, the M8 dwarf vB 10 (Berger et al. 2008) and the M9 dwarf LHS 2065 (Martín & Ardila 2001), using the appropriate χ factor from West & Hawley (2008). For these two objects equivalent widths have been measured both during quiescence and during flares[7]. For vB 10 and LHS 2065, the Hα/Hβ ratio is lower during the flare with respect to the quiescent state. The four available measurements for LHS 2065 representing a flare in its decaying phase follow, as in the case of vB 10, roughly the Hβ/Hα flux-flux relation of earlier M dwarfs in Fig. 5.

In Fig. 6, we compare our results for DENIS 1048-3956, vB 10, LHS 2065, and the early M dwarfs from MA11 to the average Balmer decrements given for "active" M dwarfs by Bochanski et al. (2007) (henceforth BWHC07). These authors defined template spectra for M dwarfs from a systematic analysis of more than 4000 spectra from the SDSS spectroscopic database. They defined "active" stars as those having $EW_{\mathrm{H}\alpha} > 1$ Å and Hα emission detected with a confidence level of at least 3σ above the noise level. If we apply the same criteria to the MA11 M dwarf sample, the total number of stars is reduced but the Balmer decrements do not change significantly. Figure 6 also shows the decrements measured by Johns-Krull et al. (1997) (henceforth JK97) for the Sun during quiescence and the range observed throughout a solar flare. In general, M dwarfs have a Hα/Hβ decrement that is more similar to solar flares than to the quiet state of the Sun. The exception is the Hα/Hβ ratio. Compared to quiescence, the solar flare has a higher Hα/Hβ ratio, while the UCDs LHS 2065 and vB 10 seem to behave the opposite way. We caution that the error bars for the measurements of vB 10, which we deliberately omit in Fig. 6, are extremely large as a result of the poorly constrained χ factors for late-M dwarfs. For LHS 2065, no uncertainties in the equivalent widths are given in the literature.

The higher values for the decrements of BWHC07 with respect to those measured by us for the MA11 sample may be due to a spectral-type dependence within the M class. The decrements of BWHC07's from Hγ/Hβ upward include only stars of spectral type M4 and later, while the MA11 sample is restricted to M0-M5 stars. However, extrapolating this apparent trend to UCD spectral types, one would expect the M9 dwarf DENIS 1048-3956 to have even higher decrements than BWHC07's stars. This is obviously not the case. In contrast, the Balmer decrements of DENIS 1048-3956 are compatible with those of the earlier-type MA11 sample. We caution that the fluxes in the Balmer decrements have been computed in different ways for the various samples. While for DENIS 1048-3956, we integrated the spectrum over the wavelengths representing the line, for both M dwarf samples (MA11 and BWHC07) the χ factor was used. BWHC07 computed the decrements from a mean template spectrum for each spectral type, while for the MA11 data we evaluated each spectrum separately and then calculated the mean of the measured decrements.

The only decrement observed for the full range of M dwarfs by BWHC07 is Hα/Hβ, which is indeed in perfect agreement with the value obtained for the MA11 stars. BWHC07 note that this flux ratio seems to become gradually stronger towards later spectral type. We display their measurements in Fig. 7 together with our results for the MA11 sample. The latter one has very large error bars owing to the small number of objects (in the range 1–4) in each spectral type bin and the error propagation into the flux ratio of the uncertainties in the χ factors. The latest spectral type for which Bochanski et al. (2007) present Balmer decrements is M8. The value for this spectral type derived from the SDSS sample is in perfect agreement with the quiescent value of vB 10. Fig. 7 also shows that our measurement for DENIS 1048-3956 extends the trend at the cool end with a sharp rise in the Hα/Hβ decrement. Although our formal error bars for DENIS 1048-3956 are considerable, the result is bolstered by the quiescent decrement of LHS 2065, which is actually a lower limit. We recall, however, that the errors for vB 10 and LHS 2065, which are not shown in the plot, are even larger than those of DENIS 1048-3956.

4.2.2. Calculated Balmer decrements

To determine the physical conditions in the region emitting the Balmer lines we calculated the flux ratios for different

[7] For the sake of consistency with the literature on Balmer decrements during flares (in particular the solar data of Johns-Krull et al. 1997) we subtracted the quiescent line fluxes from those measured during the flare obtaining in this way the "flare-only" emission and corresponding Balmer decrement. In the case of LHS 2065, where the flare is represented by three of the four available Hα/Hβ measurements, we subtracted the fluxes of the last spectrum representing the quiescence from the fluxes obtained for the three preceeding spectra.

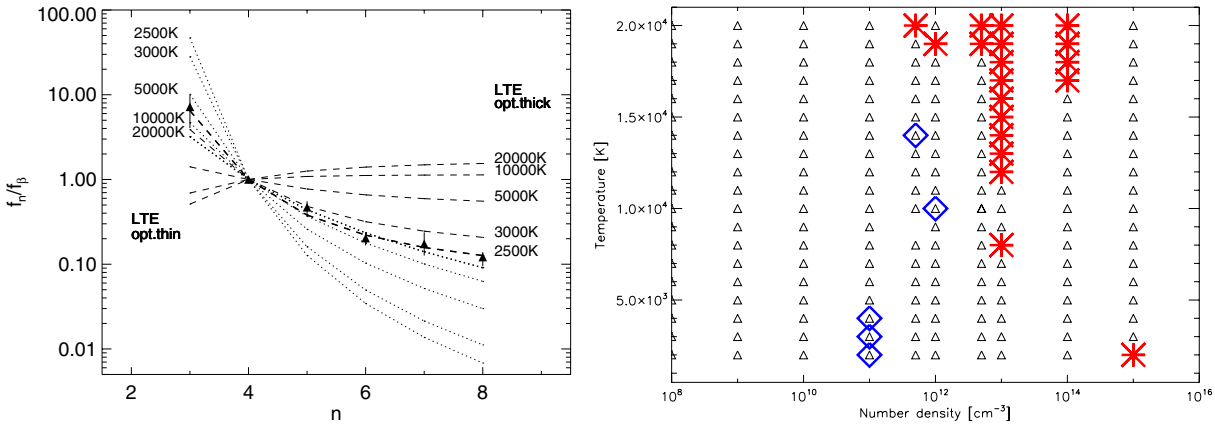

Fig. 8. Theoretical predictions for Balmer decrements: (*left*) – optically thick (dashed) and optically thin (dotted) gas in LTE and observed flux ratios for DENIS 1048-3956. For both the optically thick and the optically thin case, the model with the temperature that best fits the observed decrements is highlighted as a thick line. (*Right*) – grid of temperature and electron density for a recombining hydrogen plasma. Models compatible with the observed Balmer decrements of DENIS 1048-3956 are marked by large colored symbols: blue diamonds (Hα/Hβ) and red asterisks (the higher-n decrements).

assumptions: optically thick and optically thin gas in local thermal equilibrium (LTE) and case B recombination.

For the optically thick LTE, case we computed the Balmer flux ratios according to Eq. (1) in Bary et al. (2008) from the Planck function. Optically thin LTE level populations were described by the Boltzmann distribution. We adopted Einstein coefficients and oscillator strengths for the Balmer lines from the *National Institute of Standard & Technology Atomic Spectra Database*[8]. A range of temperatures from 2000 K to 20 000 K was explored for both optically thin and thick LTE conditions. The predicted Balmer decrements are displayed in Fig. 8 (left) together with the observed values for DENIS 1048-3956. Optically thin LTE emission describes the trend of the Balmer decrements for DENIS 1048-3956 best for a temperature of 20 000 K. Optically thick LTE plasma fits the data only for a very low temperature of 2500 K. We note that this value corresponds to the temperature in the photosphere of DENIS 1048-3956 (see Sect. 3.1).

The electron cascade and the population densities of the energy levels in recombining hydrogen plasma (case B) were determined using the method of Storey & Hummer (1995). We performed a grid of 191 models spanning temperatures in the range 2000 K to 20 000 K and number densities of electrons in the range 10^8 to 10^{15} cm^{-3}. Models were produced and fitted to all observed Balmer decrements of DENIS 1048-3956. Figure 8 (right) shows the parameter space, where each black triangle represents a model. We found no temperature/density combination that could simultaneously reproduce both the Hα/Hβ ratio and the higher Balmer decrements within the range of the observational errors given in Table 2. The Hα/Hβ decrement is more closely fit by models (blue diamonds) with lower plasma temperatures and densities compared to models that fit the other Balmer decrements (red asterisks). If the case B conditions apply, i.e. if the level populations of the plasma emitting the Balmer lines are determined by radiative cascades, Hα emission and the other Balmer lines must be produced in different regions, and Hα may be formed in a region of very low temperature.

4.3. Radio versus X-ray emission

Over the past decade, a database of sensitive X-ray and radio observations of UCDs has slowly accumulated. The relation between the emissions in these two wavebands has unveiled important differences from the X-ray/radio connection observed in low-mass GKM stars. Detailed discussions are found, e.g., in Berger (2006) and Berger et al. (2010).

Making use of data collected in previous studies, we show in Fig. 9 radio vs. X-ray luminosity for UCDs. The observations are complemented by our new X-ray measurement for DENIS 1048-3956. For the sake of enlarging the database of UCD activity, we also add unpublished X-ray observations of two UCDs that have in the past been observed in the radio band, PC 0025+0447 and DENIS 1228-1547, both plotted in green in Fig. 9. We describe these targets, the X-ray observations, and their analysis in the Appendix. Both objects were undetected in both X-rays, according to our analysis, and radio (see Berger 2002). As seen in Fig. 9, their upper limits do not provide strong constraints.

The most evident feature in Fig. 9 is the violation of the Benz-Güdel relation, first pointed out by Berger et al. (2005). Secondly, we note a dichotomy for UCDs in terms of their radio and X-ray emission: (A) In Fig. 9 we plot in red a group of objects with X-ray flares and persistent X-ray emission but no radio emission, comprising LP 412-31, LHS 2065, vB 10, Gl 569 B, and vB 8. (B) In Fig. 9 we plot in orange a group of objects with strong radio flares, mostly also with detected quiescent radio emission but no or very weak X-rays (TVLM 513-46546, 2MASS J0036159+182110, LSR J1835+3259, and possibly BRI B0021-0214). DENIS 1048-3956 (shown in green) also belongs to this latter group. LP944-20 is the only UCD for which flaring was observed in both the radio and the X-ray bands. For all other objects, no flares have been recorded so far in X-rays or radio, most of them have not yet been detected at either wavelength, and consequently they cannot (yet) be assigned to either of the two groups.

The characteristics of the radio emission of group B has been shown to be very different from that of G, K, and early-M dwarfs. While their quiescent emission may be ascribed to gyrosynchrotron radiation as in GKM stars, an additional, pulsed emission component that is highly circularly polarized has been found – TVLM 513-46546 (Hallinan et al. 2006), 2MASS J0036159+182110 (Berger et al. 2005), LSR J1835+3259 (Hallinan et al. 2008), and DENIS 1048-3956 (Burgasser & Putman 2005) – superimposed on their quiescent, non-variable emission. The periodicities of the spikes are consistent with the rotation rate of the objects implying that they

[8] The NIST Atomic Spectra Database is available at http://physics.nist.gov/PhysRefData/ASD/lines_form.html

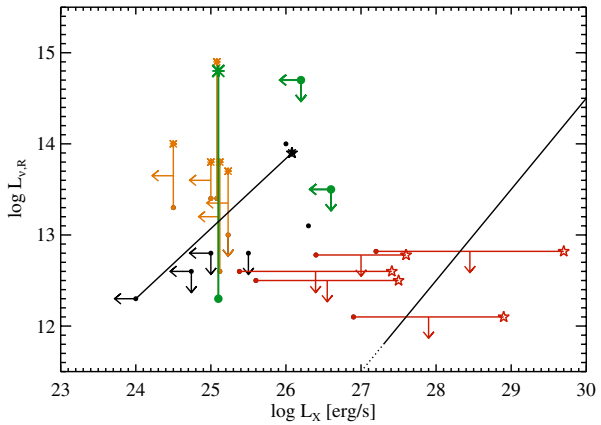

Fig. 9. Radio vs. X-ray luminosity for UCDs including DENIS 1048-3956 (green larger symbols connected by the vertical line), PC 0025+0447, and DENIS 1228-1547 (both also shown in green and larger). The Benz-Güdel-relation for more massive late-type stars is represented by the black solid line and its extrapolation to low luminosities is dotted. The lowest observed emission level of each object is shown as a circle. Two groups with distinct flaring behavior in the radio (orange with asterisks for the flares) and X-ray (red with star symbols for the flares) bands are identified. Objects that cannot be assigned to any of the groups (yet) are shown in black.

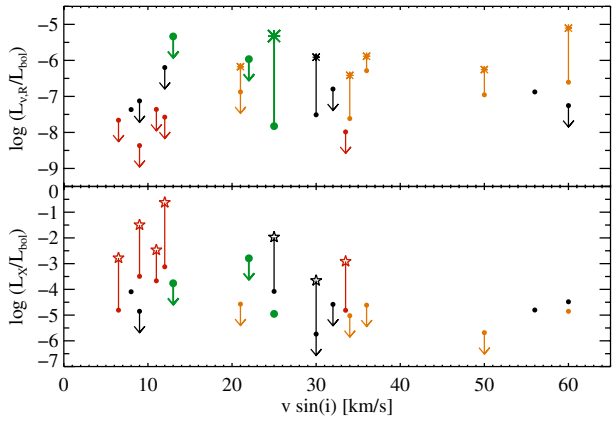

Fig. 10. Fractional radio and X-ray luminosity of UCDs vs. rotational velocity; same plotting symbols as in Fig. 9.

originate in a beaming mechanism. This radio component has been shown to be consistent with ECM instability. High inclinations were derived for TVLM 513-46546, 2MASS J0036159+182110, and LSR J1835+3259, leading Hallinan et al. (2008) to ascribe the radio detection of the ECM emission in these UCDs to a geometric selection effect. If this scenario were true, high inclination would also be expected for DENIS 1048-3956, a hypothesis to be examined by means of photometric monitoring search for its rotation period.

Group A could in principle be composed of UCDs in which the viewing conditions do not allow us to observe the ECM pulses. However, the quiescent X-ray luminosities of its members are higher than those of group B objects. It is also striking that no coherent radio emitter is a strong and flaring X-ray source. In contrast, no flaring X-ray emitter is a (strong) radio source. (The exception is LP 944-20 for which the ECM mechanism has not been explicitly confirmed.) This leads us to search for a possible origin of the apparent differences.

All group A objects except Gl 569 B are in the sample for which Reiners & Basri (2007) have searched for magnetic fields, and strong fields in the range of 1.3...3.9 kG were detected in all of them. No direct magnetic-field measurements are yet available for the group B objects with the exception of DENIS 1048-3956 (2.3 ± 0.4 kG; Reiners & Basri 2010). This observational bias is related to the ability to measure fields depending on the rotation speed. Rapid rotation makes it more difficult to detect magnetic line broadening. Figure 10 shows that stars in group A are slower rotators than those in group B. The only fast rotator in Group A, Gl 569 B, has a large uncertainty in its $v \sin i$ value. First, Zapatero Osorio et al. (2004) gave an uncertainty in ~50% on their measurement of $v \sin i$. Secondly, Gl 569 B is a spectroscopic binary and we have plotted the mean of the values measured for the two BDs (30 ± 15 and 37 ± 15 km s^{-1} for Gl 569Ba and Gl 569 Bb, respectively). Two additional UCDs exhibited X-ray flares, SCR 1845-6357 (Robrade et al. 2010) and RXS J115928.5-524717 (Robrade & Schmitt 2009), which are plotted in black with asterisks for flares in Fig. 10. While the former one has a very low limit to its quiescent X-ray emission, the latter has a quiescent X-ray detection, i.e. it has a similar X-ray behaviour to group A. Both objects have not yet been observed in the radio band.

It was recognized by Berger et al. (2008) that the radio and the X-ray emission of UCDs follow opposite trends at high rotational velocity and that fast rotators violate the Benz-Güdel relation more significantly than slow rotators. Their conclusion was that magnetic activity (as measured in the radio band) is regulated by rotation, and that the decline in X-ray emission for fast rotators is controlled by secondary effects such as inefficient plasma heating or coronal stripping. However, the X-ray detection of the fastest rotators, Kelu 1 and TVLM 513-46546, both with $v \sin i = 60$ km s^{-1} according to Mohanty & Basri (2003), argues against a suppression of X-ray emission as a result of rotation. Kelu 1 (spectral type L) is also one of the coolest objects in the sample. A possible explanation of the (apparent) absence of radio pulses in group A, in addition to the inclination effect put forth by Hallinan et al. (2008), is another selection effect related to their longer rotation periods. For $v \sin i \sim 10$ km s^{-1} and a "canonical" radius of 0.1 $R_\odot$, the maximum period is ~0.5 d, which is much longer than the typical duration of the radio observations (typically 1–3 h). In most of the radio-detected UCDs for which specific radio monitoring programs were undertaken, a pulsed component was seen. The exception is vB 10, which did not show radio bursts in 10 h of continuous monitoring with the VLA (Berger et al. 2008). However, with its low rotation of 6.5 km s^{-1}, the rotation period may be as high as 0.8 d, almost twice as long as the radio observation.

5. Summary and conclusions

We have presented the first X-ray detection of the M9 dwarf DENIS 1048-3956 ($\log L_X$ [erg/s] = 25.1) and a broad-band spectrum from the UV to the NIR from which we have redetermined its stellar parameters (spectral type = M9, $T_{\rm eff}$ = 2450 ± 50 K, $\log g$ = 4.3 ± 0.3) and kinematics (RV = −11.4 ± 2.0 km s^{-1}; UVW space motions characteristic of the young disk).

The flux-calibrated broad-band spectrum together with the X-ray data have allowed us to extend flux-flux relations between chromospheric and coronal emissions into the regime of UCDs. We used the dwarfs of early- to mid-M type from Martínez-Arnáiz et al. (2011b) as a comparison sample for which we constructed flux-flux relations between Ca II H+K, Balmer lines, and soft X-rays. The correlations differ slightly from those determined by MA11 in an analogous study that included stars in

a broader range of spectral types (F-M). We compiled data from the literature for other UCDs. Given the large range over which the relations must be extrapolated from the early-M dwarfs to the UCDs including DENIS 1048-3956, the agreement of these objects with the flux-flux relations is reasonably good. The discrepancies found for DENIS 1048-3956 include an excess of Hα and X-ray emission with respect to Ca II. Calcium measurements for other UCDs are required to verify whether this is a typical characteristic of UCDs.

We have examined the Balmer decrements for DENIS 1048-3956 up to H8. A trend of increasing Balmer decrement towards later spectral type within the M class, identified in a SDSS sample by BWHC07, is confirmed by our study in two ways: (1) We have presented the first measurement for M9 dwarfs (DENIS 1048-3956 and LHS 2065). Both objects have the largest Hα/Hβ decrements measured so far within the M class. (2) The decrements f_n/f_β with $n = 3...6$ are smaller for early-M dwarfs (MA11 sample) than for late-M dwarfs (BWHC07 sample). However, contradicting this trend, the higher-n Balmer decrements of DENIS 1048-3956 are compatible with those of the early M dwarfs from MA11 rather than with those of the (on average) later M dwarfs from BWHC07.

The observed Balmer decrements of DENIS 1048-3956 can be reproduced by an optically thick low-temperature (2500 K) plasma in LTE conditions or by an optically thin high-temperature (20 000 K) plasma in LTE conditions. The case B recombination scenario is able to reproduce the decrements Hn/Hβ for $n = 5$ and higher for a range of electron densities between 10^{12} cm^{-3} and 10^{14} cm^{-3} and temperature >10 000 K but these models cannot fit the Hα/Hβ ratio and the Hα/Hβ ratio seems to be produced in a region of lower density and temperature. For the densities and temperatures of the recombining plasma shown to describe the observed Balmer decrements from $n = 5$ upwards, one would also expect the detection of He I D emission, in contrast to our observation.

The high Hα/Hβ ratio of DENIS 1048-3956 is among the most curious findings of our study. It is this ratio that places in doubt the case B interpretation, which leads to the low temperatures for the optically thick LTE scenario, and is poorly fitted by any optically thin LTE model. That such high Hα/Hβ ratios may be realistic, and possibly even typical, for UCDs is supported by the results for vB 10 and LHS 2065 that we extracted from the literature. Nevertheless, we stress that the data for these two UCDs have very large or unknown uncertainties and, hence, the only robust measurements of the Balmer decrements in UCDs available so far are those from our flux-calibrated X-Shooter spectrum of DENIS 1048-3956.

Formally, the optically thick LTE emission provides the closest match to the Balmer lines of DENIS 1048-3956. Comparing the measured line fluxes to the blackbody flux, we estimate the line emitting area to be between 2% (for Hα) and 100% (for H8) of the stellar surface, which can be considered reasonable values to the order of magnitude. We note that virtually all cases of Balmer line analyses treated in the literature refer to flares, while for DENIS 1048-3956 we deal with non-flaring hydrogen emission. An exception where Balmer line fluxes are given for quiescent emission is the study of the M6 dwarf CN Leo by Fuhrmeister et al. (2007). For that case, the Balmer ratios H9/Hβ to H15/Hβ cannot be described by optically thick LTE plasma, and the lower Balmer lines are not available. The low temperature of the optically thick LTE emission fitting the Balmer decrements of DENIS 1048-3956 suggests that the lines are emitted from just above the photosphere. This is at odds with the common notion that the hydrogen lines in active stars are produced in the chromosphere at temperatures around ten-thousand Kelvin. The best-fitting optically thin LTE plasma indeed corresponds to such high temperatures. This model underpredicts the Hα emission but, all in all, seems to be more plausible than the low-temperature optically thick case.

DENIS 1048-3956 clearly possesses a corona manifested by its X-ray detection, i.e. hot material of MK temperatures is present. Further complicating the picture, the X-ray emitting plasma of DENIS 1048-3956 may not be associated with the radio structures: Ravi et al. (2011) ascribed the gyrosynchrotron radio component to emission from electrons streaming out in open field lines that cannot confine coronal plasma, while the pulsed radio component represents ECM emission (Burgasser & Putman 2005), i.e. it has a physically different origin from the X-ray photons.

Our X-ray detection of DENIS 1048-3956 also adds a new data point to the poorly sampled group of stars with sensitive X-ray and radio observations. We tentatively identify two subgroups of UCDs, X-ray flaring but radio faint objects with low rotation rates on the one hand and radio bursting but X-ray faint fast rotators on the other hand. DENIS 1048-3956 belongs to the latter class. At present, it remains unclear whether this distinction corresponds to two physical populations or is produced by observational biases.

Appendix A: New X-ray observations of UCDs

A.1. PC 0025+0447

PC 0025+0447 was identified by Schneider et al. (1991) as an M star with outstanding Hα emission. On the basis of the lithium test, Martín et al. (1999a) concluded that this M9.5 object is a BD with age <1 Gyr. Variable veiling was ascribed to activity, given the absence of a NIR excess that would indicate an accretion disk. What makes PC 0025+0447 particular among the UCDs is that its very high levels of Hα activity are persistent without any evidence of flaring.

PC 0025+0447 was observed with *Chandra* ACIS-S on 7 Dec. 2001 for 66 ks (Obs-ID 2579). We analysed the data with standard CIAO[9] tools. A description of the data reduction steps and calculation of upper limits can be found e.g. in Stelzer et al. (2010).

No X-ray source is associated with PC 0025+0447. We derived a 95% confidence level for the count-rate upper limit of 9.6×10^{-5} cts/s in the 0.3−8 keV band. Assuming a one-temperature thermal spectrum of $\log T\,[\mathrm{K}] = 6.85$, PIMMS yields the count-to-flux conversion factor, which, when combined with the upper limit count rate, gives the flux limit. The distance of PC 0025+0447 had been reported to be 72 pc (Dahn et al. 2002), and we obtained $\log L_\mathrm{x}\,[\mathrm{erg/s}] < 26.2$, one order of magnitude below the previous upper limit from *ROSAT* (Neuhäuser et al. 1999). With a bolometric luminosity of $\log(L_\mathrm{bol}/L_\odot) = -3.62$ (Dahn et al. 2002), the fractional X-ray luminosity is $\log(L_\mathrm{x}/L_\mathrm{bol}) < -3.8$.

A.2. DENIS 1228-1547

DENIS 1228-1547 stood out among the first stars identified by DENIS as being relatively young. An upper limit to its age of 1 Gyr and a maximum mass of 55 M_jup was inferred from its

[9] CIAO is the *Chandra* Interactive Analysis of Observations package provided by the *Chandra* X-ray Center (http://cxc.harvard.edu/ciao/index.html).

lithium absorption (Martin et al. 1997). DENIS 1228-1547 was classified as L5 spectral type (Koerner et al. 1999). It was resolved into a nearly equal-mass binary (Martin et al. 1999b; Brandner et al. 2004) with a separation of ~0.28″, i.e. unresolvable by any present-day X-ray instrument.

An archived *XMM-Newton* observation (ObsID 0002740601 and ObsID 0002740301) comprises 5.7 ks of EPIC/pn exposure and 11.3 ks of EPIC/MOS exposure. We analysed the EPIC/pn data with standard *XMM-Newton* SAS tools. The highest sensitivity could be obtained by merging the data from the three instruments. However, the unknown relative sensitivity introduces a significant uncertainty. EPIC/MOS is typically three times less sensitive than EPIC/pn, but this depends on the source spectrum. Therefore, despite the shorter exposure time, we concentrate on EPIC/pn data only.

DENIS 1228-1547 was not detected in this X-ray observation. Analogous to the case of PC 0025+0447, we derived a 95% confidence upper limit for the count rate (0.007 cts/s) and using the same assumptions for the spectral shape we obtained the flux limit. The trigonometric parallax of DENIS 1228-1547 gives a distance of 20.2 pc (Dahn et al. 2002), yielding an X-ray luminosity of $\log L_{\rm x}$ [erg/s] < 26.6 and with $\log(L_{\rm bol}/L_{\odot}) = -4.19$ (Dahn et al. 2002) its fractional X-ray luminosity is $\log(L_{\rm x}/L_{\rm bol}) < -2.8$.

Acknowledgements. We would like to recognize valuable input from an anonymous referee. B.S. wishes to thank Fabrizio Bocchino for hot discussions on cool stars. B.S. acknowledges financial contribution from the agreement ASI-INAF I/009/10/0. K.B. acknowledges financial support from the INAF Postdoctoral fellowship. This work is based on observations obtained with *XMM-Newton*, an ESA science mission with instruments and contributions directly funded by ESA Member States and NASA, and on observations made with ESO Telescopes at the VLT on the Paranal Observatory under programme ID ⟨085.C-0238⟩.

References

Alcalá, J. M., Stelzer, B., Covino, E., et al. 2011, Astron. Nachr., 332, 242
Allard, F., Homeier, D., & Freytag, B. 2010 [arXiv:1011.5405]
Baraffe, I., Chabrier, G., Barman, T. S., Allard, F., & Hauschildt, P. H. 2003, A&A, 402, 701
Barrado, D., Stelzer, B., Morales-Calderón, M., et al. 2011, A&A, 526, A21
Bary, J. S., Matt, S. P., Skrutskie, M. F., et al. 2008, ApJ, 687, 376
Basri, G., Mohanty, S., Allard, F., et al. 2000, ApJ, 538, 363
Berger, E. 2002, ApJ, 572, 503
Berger, E. 2006, ApJ, 648, 629
Berger, E., Rutledge, R. E., Reid, I. N., et al. 2005, ApJ, 627, 960
Berger, E., Basri, G., Gizis, J. E., et al. 2008, ApJ, 676, 1307
Berger, E., Basri, G., Fleming, T. A., et al. 2010, ApJ, 709, 332
Bochanski, J. J., West, A. A., Hawley, S. L., & Covey, K. R. 2007, AJ, 133, 531
Brandner, W., Martín, E. L., Bouy, H., et al. 2004, A&A, 428, 205
Burgasser, A. J., & Putman, M. E. 2005, ApJ, 626, 486
Costa, E., Méndez, R. A., Jao, W.-C., et al. 2005, AJ, 130, 337
Crespo-Chacón, I., Montes, D., García-Alvarez, D., et al. 2006, A&A, 452, 987
Dahn, C. C., Harris, H. C., Vrba, F. J., et al. 2002, AJ, 124, 1170
Delfosse, X., Forveille, T., Martín, E. L., et al. 2001, A&A, 366, L13
Doyle, J. G. 1989, A&A, 218, 195
Frasca, A., & Catalano, S. 1994, A&A, 284, 883
Fuhrmeister, B., & Schmitt, J. H. M. M. 2004, A&A, 420, 1079
Fuhrmeister, B., Liefke, C., & Schmitt, J. H. M. M. 2007, A&A, 468, 221
Gizis, J. E., Monet, D. G., Reid, I. N., et al. 2000, AJ, 120, 1085
Güdel, M. 1994, ApJS, 90, 743
Hall, J. C. 1996, PASP, 108, 313
Hallinan, G., Antonova, A., Doyle, J. G., et al. 2006, ApJ, 653, 690
Hallinan, G., Antonova, A., Doyle, J. G., et al. 2008, ApJ, 684, 644
Hawley, S. L., Gizis, J. E., & Reid, I. N. 1996, AJ, 112, 2799
Isobe, T., Feigelson, E. D., Akritas, M. G., & Babu, G. J. 1990, ApJ, 364, 104
Johns-Krull, C. M., Hawley, S. L., Basri, G., & Valenti, J. A. 1997, ApJS, 112, 221
Koerner, D. W., Kirkpatrick, J. D., McElwain, M. W., & Bonaventura, N. R. 1999, ApJ, 526, L25
Kruse, E. A., Berger, E., Knapp, G. R., et al. 2010, ApJ, 722, 1352
Kuntz, K. D., Harrus, I., McGlynn, T. A., Mushotzky, R. F., & Snowden, S. L. 2008, PASP, 120, 740
Lee, K.-G., Berger, E., & Knapp, G. R. 2010, ApJ, 708, 1482
Liebert, J., Kirkpatrick, J. D., Cruz, K. L., et al. 2003, AJ, 125, 343
López-Santiago, J., Montes, D., Gálvez-Ortiz, M. C., et al. 2010, A&A, 514, A97
Martín, E. L., & Ardila, D. R. 2001, AJ, 121, 2758
Martin, E. L., Basri, G., Delfosse, X., & Forveille, T. 1997, A&A, 327, L29
Martín, E. L., Basri, G., & Zapatero Osorio, M. R. 1999a, AJ, 118, 1005
Martin, E. L., Brandner, W., & Basri, G. 1999b, Science, 283, 1718
Martín, E. L., Delfosse, X., Basri, G., et al. 1999c, AJ, 118, 2466
Martínez-Arnáiz, R., López-Santiago, J., Crespo-Chacón, I., & Montes, D. 2011a, MNRAS, 414, 2629
Martínez-Arnáiz, R., López-Santiago, J., Crespo-Chacón, I., & Montes, D. 2011b, MNRAS, 417, 3100
Modigliani, A., Goldoni, P., Royer, F., et al. 2010, in SPIE Conf. Ser., 7737
Mohanty, S., & Basri, G. 2003, ApJ, 583, 451
Mohanty, S., Basri, G., Shu, F., Allard, F., & Chabrier, G. 2002, ApJ, 571, 469
Montes, D., López-Santiago, J., Gálvez, M. C., et al. 2001, MNRAS, 328, 45
Neuhäuser, R., Briceño, C., Comerón, F., et al. 1999, A&A, 343, 883
Ravi, V., Hallinan, G., Hobbs, G., & Champion, D. J. 2011, ApJ, 735, L2
Reid, I. N., Kirkpatrick, J. D., Liebert, J., et al. 2002, AJ, 124, 519
Reiners, A., & Basri, G. 2007, ApJ, 656, 1121
Reiners, A., & Basri, G. 2009, ApJ, 705, 1416
Reiners, A., & Basri, G. 2010, ApJ, 710, 924
Reiners, A., Basri, G., & Browning, M. 2009, ApJ, 692, 538
Robrade, J., & Schmitt, J. H. M. M. 2009, A&A, 496, 229
Robrade, J., Poppenhaeger, K., & Schmitt, J. H. M. M. 2010, A&A, 513, A12
Roeser, S., Demleitner, M., & Schilbach, E. 2010, AJ, 139, 2440
Rosner, R., Golub, L., & Vaiana, G. S. 1985, ARA&A, 23, 413
Rutten, R. G. M., Zwaan, C., Schrijver, C. J., Duncan, D. K., & Mewe, R. 1989, A&A, 219, 239
Schmidt, S. J., Cruz, K. L., Bongiorno, B. J., Liebert, J., & Reid, I. N. 2007, AJ, 133, 2258
Schmitt, J. H. M. M., & Liefke, C. 2004, A&A, 417, 651
Schmitt, J. H. M. M., Fleming, T. A., & Giampapa, M. S. 1995, ApJ, 450, 392
Schneider, D. P., Greenstein, J. L., Schmidt, M., & Gunn, J. E. 1991, AJ, 102, 1180
Schönrich, R., Binney, J., & Dehnen, W. 2010, MNRAS, 403, 1829
Schrijver, C. J., & Rutten, R. G. M. 1987, A&A, 177, 143
Schrijver, C. J., Dobson, A. K., & Radick, R. R. 1989, ApJ, 341, 1035
Siess, L., Dufour, E., & Forestini, M. 2000, A&A, 358, 593
Stelzer, B., Micela, G., Flaccomio, E., Neuhäus er, R., & Jayawardhana, R. 2006, A&A, 448, 293
Stelzer, B., Flaccomio, E., Briggs, K., et al. 2007, A&A, 468, 463
Stelzer, B., Scholz, A., Argiroffi, C., & Micela, G. 2010, MNRAS, 408, 1095
Storey, P. J., & Hummer, D. G. 1995, MNRAS, 272, 41
Talavera, A. 2009, Ap&SS, 320, 177
West, A. A., & Hawley, S. L. 2008, PASP, 120, 1161
Zapatero Osorio, M. R., Lane, B. F., Pavlenko, Y., et al. 2004, ApJ, 615, 958